Drop-In Test Structure to Evaluate Residual Stress in Conformally Grown Films

Naoto Usami , *Member, IEEE*, Etsuko Ota, Akio Higo , *Member, IEEE*, Takeshi Momose , and Yoshio Mita , *Senior Member, IEEE*

Abstract—We propose and demonstrate a drop-in test structure to visualize and measure the residual stress in the conformally deposited film. For reliable device process of microsystems (such as 3-D MEMS), the residual stress must be controlled through quantitative evaluation at each deposition step. A small drop-in test structure placed near the main sample is suitable for monitoring film characteristics. We developed a free-standing rotating beam stress sensor as the drop-in test structure to visualize and measure the residual stress in conformally deposited films with no additional processes. The dimensions of the developed drop-in test structure chips were 5 mm × 10 mm. For a demonstration, Cu supercritical fluid deposition (SCFD) was performed over the test structure chips under a couple of conditions. The residual stresses in SCFD Cu films were successfully extracted by equation-based analysis.

Index Terms—Residual stress, test structure, conformal deposition, MEMS, SCFD, ALD.

I. INTRODUCTION

METALIZATION and/or insulation on high aspect ratio microstructures (HARMS [1]) and suspended structures is a major concern in the research of the micro electromechanical system (MEMS) technology. Recently, instead of physical vapor deposition with poor step coverage, studies have utilized several conformal deposition techniques, such as atomic layer deposition (ALD) [2], [3], electroless plating [4], [5], electroplating [6], and supercritical fluid deposition (SCFD) [7], [8] for metalization and/or insulation of HARMS.

Residual stress is one of the factor affecting reliability of deposited films on HARMS. It is related to adhesion and

crack occurrence [9], [10]. The residual stress of conformally deposited films also causes deformation of suspended MEMS structures [3]. Therefore, the monitoring of the residual stress in deposited films can contribute to the development of reliable processes for metalized/insulated HARMS.

However, the measurement of residual stress in samples developed in lab-level experimental deposition systems is difficult because of the small size of the samples (typically approximately $1\,cm^2$). Furthermore, the lab-level deposition systems used in the process-development phase are frequently unstable. The widely utilized wafer curvature technique [11] has low sensitivity for small-sized samples. Although a typical X-ray diffraction (XRD) method requires only millimeter-scale areas without damage to the films, stress analysis using the XRD data requires sufficient *a priori* knowledge regarding the characteristics and quality of the deposited film [12]. The electron backscattered diffraction pattern (EBSD) method is also a nondestructive and area-saving technique [13]. However, its measurement result is strongly influenced by surface conditions. In addition, the applicable materials for the typical XRD and EBSD techniques are limited to crystals. The focused-ion-beam-based method [14] is a powerful technique for evaluating the residual stress of thin films. However, its applicable thickness is limited to several hundreds of nanometers [12]. Another method is surface micromachining, in which strain gauges [15] and rotating strain sensors [16] are used to evaluate the stress of a film under test (FUT). However, minimum thickness is required for the material under test to allow it to stand independently. The value is typically in hundreds of nanometers, and it does not necessarily match the request from the process engineers (e.g., they may want to characterize the stress of a < 50-nm-thick film). This is a critical drawback.

Therefore, in this study, we propose a novel drop-in test structure to characterize the residual stress in the conformal deposited film. As shown in Fig. 1, the small test structure chip is dropped adjacent to the main sample in the small experimental reactor. Our rotation beam stress sensor can be utilized to evaluate the compressive or tensile force induced by the deposited FUT. Only a simple optical microscopic image is required for the measurement. The estimation process of the residual stress value requires only the thickness value of the film. No mechanical (Young' modulus), chemical, or physical material information is required. The chip can be used for consecutive deposition processes. By obtaining an optical image after each deposition step, the process engineer can identify the stress information for each layer.
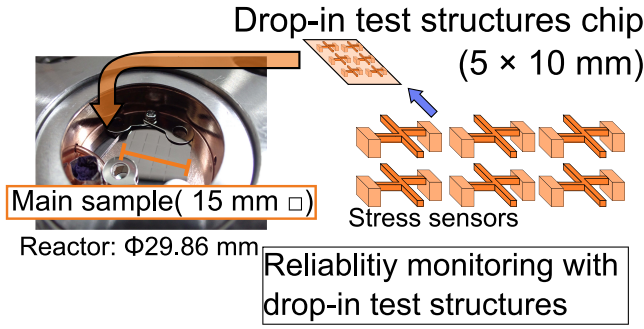
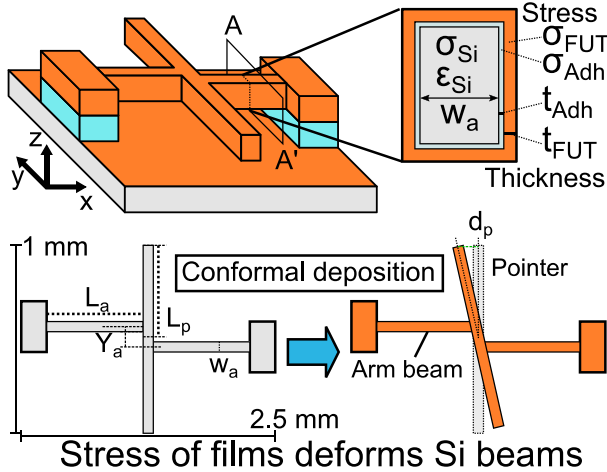Fig. 1. Residual stress evaluation by utilizing the proposed drop-in test structure.

Fig. 2. Rotating beam stress sensor for conformal deposition. Residual stress in deposited films deforms the arm beams and rotates the pointer.
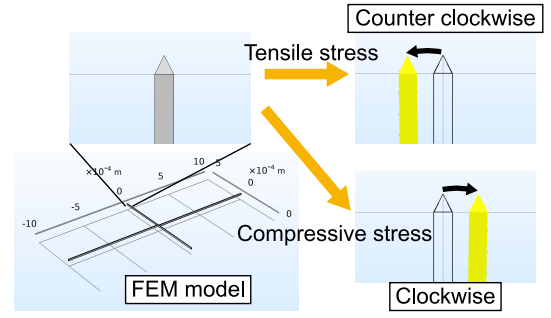

Fig. 3. FEM simulation of rotating beam stress sensor to present working principle. Tensile stress rotates the pointer counterclockwise, and compressive stress rotates it clockwise.

II. STRESS SENSOR FOR DROP-IN TEST STRUCTURE

A. Design of Rotating Beam Stress Sensor

The chip area allowed for the drop-in test structure is as small as $5 \times 10 \text{ mm}^2$. No additional process is applicable on such a small chip. We propose the use of a Si stress sensor for conformal deposition systems. The test structure was designed by referring to the rotating beam test structures [16], [17]. Conventional rotating beam test structures were utilized to measure the residual strain of thick films, such as electroplated metal films [18], [19]. The thick film was patterned into a cross beam shape, and the structure was released by an undercut process (known as the MEMS releasing process). As soon as the structure is detached from the substrate, the beam rotates according to the stress in the film. The residual stress of the released materials is directly observed through the rotation angle [20]. In this section, we focus on the characteristic that the stress in the film under test is converted to the rotation angle.

Fig. 2 depicts the schematic of our proposed rotating beam stress sensor, which is composed of suspended Si beams. To start the test, the chip was put in the deposition chamber of the FUT (we call it *drop-in*). After the deposition, the residual stress induces strain in the Si arm beams, and this appears as the pointer's rotation. We proceeded with numerical

calculation by finite element method (FEM) to investigate how the proposed sensor works. We utilized COMSOL software for the calculation. Fig. 3 shows the results of FEM calculation. We induced tensile and compressive stress (200 MPa) to 100-nm-thick FUT in the simulations. The tensile stress of the FUT rotates the pointer counterclockwise, and the compressive stress rotates the pointer clockwise. Therefore, our stress sensor can visualize the residual stress in the conformally deposited film. Because the rotation is caused by the total force derived from the residual stress in the deposited film, the rotation reflect the three-dimensional (3D) structure of the deposited film, including the sidewalls. This is the unique characteristic and critical advantage of our proposed test structure as compared to existing methods such as XRD and/or EBSD, because they can only measure stress on planar surfaces. In addition, our proposed stress sensor is applicable to any materials, without knowing its chemical or physical characteristics (required for XRD and/or EBSD), because the mechanical stress of the FUT can be directly visualized.

B. Analytical Model of Proposed Rotating Beam Stress Sensor

The output of the proposed stress sensor as displacement provides residual stress information through strain in the Si arm beams. Therefore, the stress sensor must be structurally analyzed. Herein, we derive the relationship between the stress in the FUT σ_{FUT} and strain ϵ_a in the Si arms. According to a balance of internal forces in the cross section of the arm beam in the x-axis orientation,

$$S_a \sigma_{xa} + \sum_k S_{\text{Adh}\,k} \sigma_{x\text{Adh}\,k} + \sigma_{\text{FUT}} S_{\text{FUT}} = 0 \qquad (1)$$

where S_a, $S_{\text{Adh}\,k}$, and S_{FUT} represent the cross-sectional areas of the Si arm beam, k-th adhesion layer, and FUT, respectively. σ_{xa}, $\sigma_{x\text{Adh}\,k}$, and $\sigma_{x\text{FUT}}$ are x-axis residual stress in Si arm beam, k-th adhesion layer, and FUT, respectively.

Next, we focused on difference before-and-after deposition of FUT. We assumed that the influence of FUT deposition on the adhesion layers is negligible, which means that the residual stress in the adhesion layers $\sigma_{x\text{Adh}\,k}$ are not changed by FUT deposition. Then, the variation of the x-axis stress in the arm $\Delta\sigma_{xa}$ is expressed as follow:

$$S_a \Delta\sigma_{xa} + \sigma_{\text{FUT}} S_{\text{FUT}} = 0 \qquad (2)$$
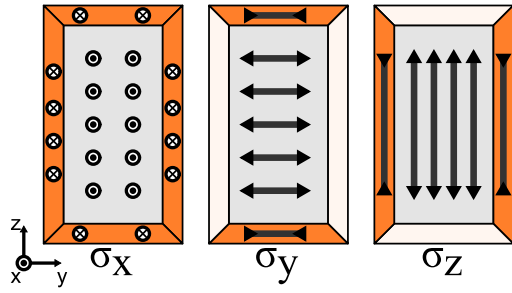
Fig. 4. Balance of internal forces derived from stress in the cross section of the arm beam. Each-axial component of stress in the arm is totally balanced to that in parallel-deposited FUT (colored area).

where $\Delta\sigma_{xa}$ is the difference in the x-axis component of residual stress before and after deposition of FUT. There are closed-form relationships for stress in y- and z-axis orientation. As shown Fig. 4, only parallel parts of FUT affect stress in the arm on y- and z-direction. Then,

$$S_a \Delta\sigma_{ya} + \sigma_{FUT} S_{yFUT} = 0 \tag{3}$$
$$S_a \Delta\sigma_{za} + \sigma_{FUT} S_{zFUT} = 0 \tag{4}$$

S_{yFUT} and S_{zFUT} are the areas that affect to the y- and z-axis component of stress in the arm, respectively. As shown Fig. 4, the total of S_{yFUT} and S_{zFUT} is equal to S_{FUT}. Then,

$$S_{yFUT} + S_{zFUT} = S_{FUT} \tag{5}$$

The relationship among σ_{xa}, σ_{ya} and σ_{za} is derived from Eq. (2)–(5) as follows:

$$S_a\left(\Delta\sigma_{ya} + \Delta\sigma_{za}\right) = -\left(S_{yFUT} + S_{zFUT}\right)\sigma_{FUT} \tag{6}$$
$$= -S_{FUT}\sigma_{FUT} \tag{7}$$

By comparing between Eq. (2) and Eq. (7),

$$\Delta\sigma_{xa} = \Delta\sigma_{ya} + \Delta\sigma_{za} \tag{8}$$

Next, we focus on the design parameters of stress sensors. S_a and S_{FUT} can be expressed with designed arm beam width, w_a, as follows:

$$S_a = hw_a + S'_a \tag{9}$$
$$S_{FUT} = 2t_{FUT}(w_a + h) + S'_{FUT} \tag{10}$$

where h is the thickness of the Si beams, t_{FUT} is the thickness of the FUT. S'_a is derived from the manufacturing error in the arm width e'_a and expressed as $S'_a = he'_a$. e'_a can be measured from the optical images of the fabricated samples. S'_{FUT} is a constant value that includes discrepancies of perimeter between the actual cross section of the fabricated arm and a pure rectangle, which is derived from sidewall scalloping. From the above-mentioned discussion, the following equation holds:

$$\Delta\sigma_{xa} = -2\frac{t_{FUT}\sigma_{FUT}}{h}\frac{w_a + h + \frac{S'_{FUT}}{2t_{FUT}}}{w_a + e'_a} \tag{11}$$

The minus sign shows that the residual stress in FUT induces opposite-orientation stress in the Si arm beam. It is coherent to the FEM simulation results in Fig. 3.

Next step is conversion from stress to deformation of the sensor. The relation between difference of stress and that of axial-orientation strain $\Delta\varepsilon_a$ in the arm beam is expressed as follow:

$$E_{Si}\Delta\varepsilon_a = \Delta\sigma_{xa} - \nu_{Si}\left(\Delta\sigma_{ya} + \Delta\sigma_{za}\right) \tag{12}$$

ν_{Si} is Poisson ratio of Si. According to Eq. (8),

$$E_{Si}\Delta\varepsilon_a = (1 - \nu_{Si})\Delta\sigma_{xa} \tag{13}$$

Therefore, Eq. (11) can be expressed as:

$$\Delta\varepsilon_a = -2\frac{(1 - \nu_{Si})t_{FUT}\sigma_{FUT}}{hE_{Si}}\frac{w_a + h + \frac{S'_{FUT}}{2t_{FUT}}}{w_a + e'_a} \tag{14}$$

$\Delta\varepsilon_a$ can be calculated from the rotation angle $\Delta\theta$, and therefore the measured displacements $d_p = L_p\Delta\theta$. In small strain region, the relationship between $\Delta\varepsilon_a$ and $\Delta\theta$ is expressed as follows [21]:

$$\Delta\theta = -\frac{2L_a^2\Delta\varepsilon}{Y_a\left(L_a + \frac{4w_a^2}{3Y_a^2}L_a\right)} \tag{15}$$

Since the schematic of the rotation beam structure in [21] is mirror symmetric to ours, the minus sign was added in Eq. (15). In this study, we derived the relationship between the distance and width of arms in $Y_a = 2w_a$, as follows:

$$d_p = L_p\Delta\theta = -\frac{3L_aL_p}{4w_a}\Delta\varepsilon \tag{16}$$

Eq. (14) can be transformed to d_p versus w_a by using Eq. (16):

$$d_p = \alpha\frac{w_a + h + \beta}{w_a(w_a + e'_a)} \tag{17}$$
$$\alpha = \frac{3(1 - \nu_{Si})L_aL_p}{2E_{Si}h}t_{FUT}\sigma_{FUT} \tag{18}$$
$$\beta = \frac{S'_{FUT}}{2t_{FUT}} \tag{19}$$

where film thickness t_{FUT} can be measured through various methods, such as cross-sectional SEM images, and ν_{Si} and E_{Si} are parameters, the values of which are obtained from the material tables. Therefore, α only includes one unknown value σ_{FUT}. The series analysis revealed the relationship between residual stress σ_{FUT}, output d_p, and the design parameters of our stress sensor: length of arm L_a, length of pointer L_p, thickness of arm h, and series of arm width w_a.

C. Numerical Analysis of the Stress Sensor

Now, we discuss the characteristics of our rotating beam stress sensors by numerical studies. The utilized parameters of the rotating beam sensor for series calculation were as follows: beam length, $L_a = 1000\,\mu m$, pointer length, $L_p = 500\,\mu m$, and pointer width $w_p = 4\,\mu m$. The thickness of device layer, h, was $14.5\,\mu m$. Since the orientation of the deformation of the arm beam is 110, the Si elastic module E_{Si} and Poisson's ratio ν_{Si} were set to 170 GPa and 0.28 from a material table, respectively.
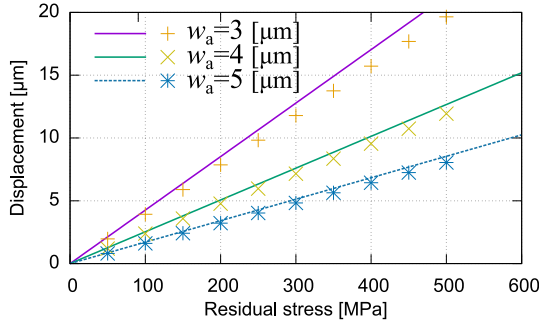
Fig. 5. Comparison between results of FEM and analytical models in Eq. (17). Lines presents calculated results of our analytical model and points presents those of FEM.
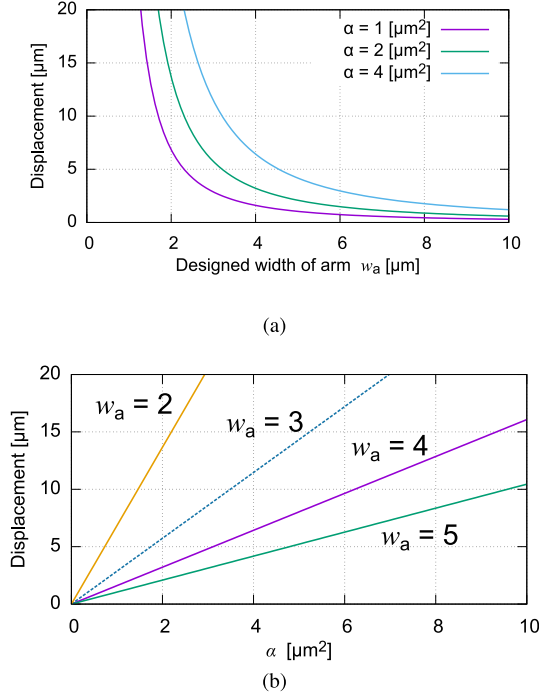

(a)

(b)

Fig. 6. Calculation of (a) w_a vs. displacement d_p under different α values, and (b) α vs. displacement d_p under different w_a values using Eq. (17). α is proportional to the product of residual stress and thickness of FUT.

Firstly, we proceeded with validation of our analytical model Eq. (17) by comparison to FEM calculation. The fabrication error terms β and e_a' in our analytical model were set to zero. Fig. 5 shows the comparison between the analytical model and FEM. The linearity in residual stress can be seen in both of our analytical model and FEM. Although the values of the analytical model are always larger than those of FEM, their systematic error are smaller than 10%. These results presents that our analytical model is reliable enough to utilize for simple evaluation.

Next, we studied parameter sensitivity in Eq. (17). We calculated the influence of the parameters on displacement d_p. Nominal values of parameters in this analysis were as follows: $\alpha = 2\,\mu m^2$, $\beta = 4\,\mu m$, $e_a' = -0.5\,\mu m$.

α is the most important parameter in Eq. (17). It is proportional to the production of thickness t_{FUT} and residual stress σ_{FUT}. Therefore, the investigation of α is the key point to know the performance of the proposed stress sensor. Fig. 6 shows

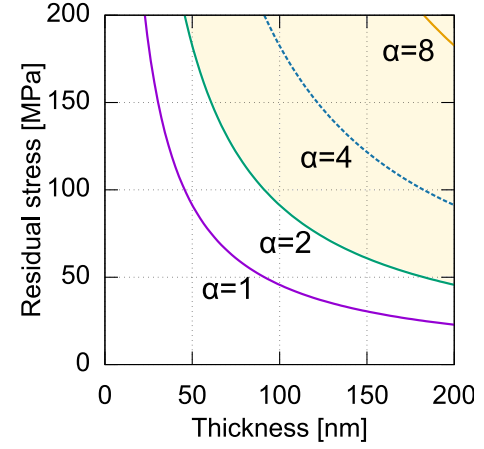Fig. 7. Calculation of film thickness t_{FUT} vs. residual stress σ_{FUT} under different α [μm^2] values from Eq. (18). Colored area corresponds to $\alpha > 2$ [μm^2].
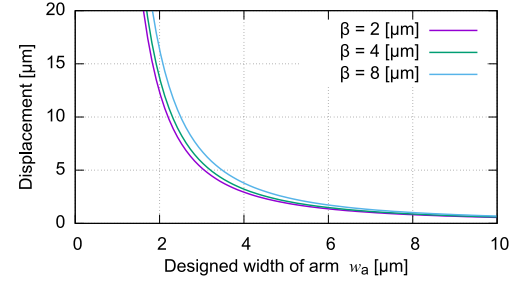

Fig. 8. Calculation of w_a vs. displacement d_p using Eq. (17) under different β values that is error of perimeter derived from scalloping of sidewall.

the dependence of displacement d_p on α in Eq. (18). As d_p is proportional to α (Eq. (17)), the variation of α strongly affects the curve of w_a vs. d_p as shown in calculation results under different α values in Fig. 6(a). Fig. 6(b) shows the calculated results of α vs. displacement d_p. A smaller w_a causes a larger inclination of the curves. Therefore, narrow-arm sensors have good sensitivity for α, and consequently, for the residual stress.

Fig. 7 presents constant α curves for thickness t_{FUT} vs. residual stress σ_{FUT} plane under the adopted design. As shown in Fig. 6, a smaller value of α provides a smaller displacement and a flatter curve of w_a vs. d_p; this prevents the precise estimation of α values. For example, displacements d_p of the sensor with $w_a = 4.5$ and $w_a = 5$ under $\alpha = 1$ were calculated as 0.8 and 0.7 μm, respectively. This difference is smaller than the error of the optical measurements. Therefore, the operating range of the adopted design roughly corresponds to the $\alpha > 2$ range in colored area of Fig. 7. This indicates that the adopted design of our proposed stress sensor can be used to evaluate the residual stress in films thinner than 100 nm; this indicates the unique characteristic of our sensor in comparison with other conventional MEMS strain/stress sensors that require sufficient thickness to stand independently.

Fig. 8 presents the dependence of displacement d_p on the discrepancy of beam perimeter β. Fig. 8 shows the calculation results of w_a vs. d_p under different β values. The difference in β has much smaller influence on d_p than that of α.
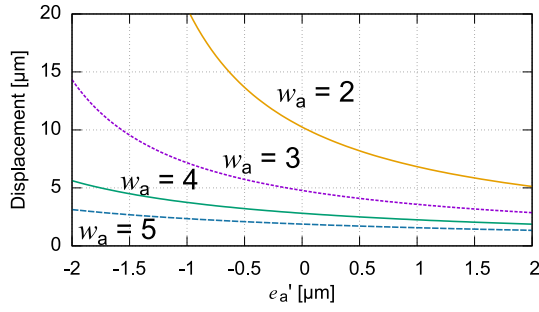
Fig. 9. Calculation of fabrication error of arm width e'_a vs. displacement d_p under different w_a values using Eq. (17).
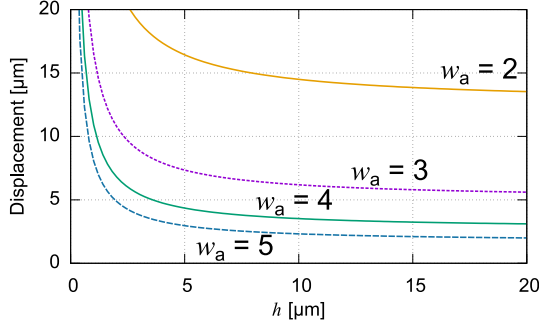

Fig. 10. Calculation of Si thickness h vs. displacement d_p under different w_a values using Eq. (17).

Fig. 9 presents the calculated results of the arm-width fabrication error, e'_a, vs. displacement d_p; d_p strongly depends on e'_a under a small w_a value. In other words, the sensitivity and correctness of the analysis display a trade-off. In the actual analysis, e'_a is derived from the optical images of the fabricated sensors, which contain submicron-order errors. Therefore, we did not adopt very-narrow-arm sensors, for example, those with $w_a < 3\,\mu$m.

Next, we focus on the design parameters; beam length, L_a, pointer length, L_p and thickness of device layer h. α is proportional to L_a and L_p as shown in Eq. (18). Although larger values of L_a and L_p simply provide larger values of α and better sensitivity on residual stress, a larger area is required for a single stress sensor on the drop-in test structure chips. An increase in the number of sensors on the one same chip can contribute to the correct estimation of α values; this also requires an additional area. Therefore, a design trade-off exists between L_a, L_p, and number of sensors.

The influence of thickness h is more complex than those of other design parameters. As β is derived from the roughness of the sidewall, its value is affected by h. According to another work using our etching machine, increment ratio of perimeter due to scalloping was 0.2–0.4 [22]. Therefore, we fixed the ratio between β and h as $\beta = 0.3\,h$. Fig. 10 presents the calculated results of thickness h vs. displacement d_p. The dependence of d_p on h saturates in higher h regions. A smaller h value decreases the uncertainty of β, and increases the value of d_p. However, the lack of thickness causes sticking in the series fabrication process.

To consider the series analysis and discussion, we adopted the following designs for the stress sensor and drop-in test
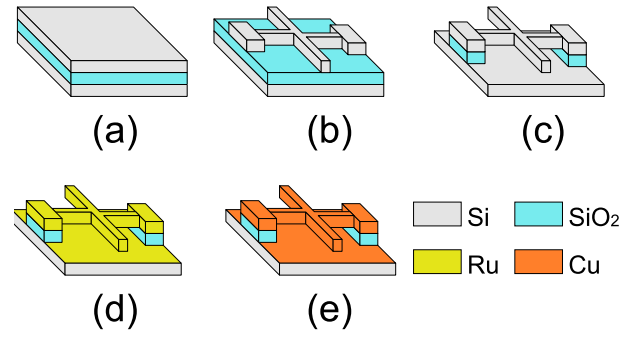

Fig. 11. Experimental flow for demonstration of rotating beam stress sensor. (a) Preparation of SOI. (b) Patterning device layer. (c) Releasing of beams. (d) Ru/TiO$_2$/SiO$_2$ ALD as adhesion layer on Si surface. (e) Cu SCFD on the Ru surface.

structure chip. One drop-in test structure chip contains six rotating beam sensors with different widths and separation of arm beams. Arm beam widths w_a and separation Y_a were taken as 3, 3.5, 4, 4.5, 5, 5.5 μm, and 6, 7, 8, 9, 10, 11 μm ($Y_a = 2w_a$), respectively. The design parameters of the rotating beam sensor is same as those utilized in above calculation: beam length, $L_a = 1000\,\mu$m; pointer length, $L_p = 500\,\mu$m, and pointer width = 4 μm. The thickness of device layer, h, was 14.5 μm. In the adopted design, the proposed stress sensor can evaluate FUT with colored thickness-stress area in Fig. 7. The measurement range includes 100 nm vs. 100 MPa that is in the range of CVD [23] and PVD [24], and 10 nm vs. 1 GPa that is in the range of ALD [25].

III. EXPERIMENTAL DESIGN AND FABRICATION

To demonstrate our proposed method, we utilized the SCFD experimental systems in [26]. SCFD is a promising technology for realizing metallic microstructures [27], [28]. SCFD has a high step coverage and high deposition rate according to supercritical fluid characteristics of high density, low viscosity, and high diffusivity [29]. SCFD has been utilized for the fabrication process of HARMS: high-aspect-ratio wiring [30], coating on complex 3D structures [31], via filling [32] and metalization of suspended structures [8]. As presented in various studies, SCFD is a powerful technology for advanced MEMS and semiconductor devices. However, its system is still utilized only at the laboratory level. To utilize SCFD for practical applications, its reliability must be improved. Although several reliability-related studies on SCFD have been reported [33], [34], [35], [36], residual stress in SCFD films has not been reported, except for our previous ICMTS conference work [37]. Therefore, investigation of residual stress in SCFD films is essential for their practical implementation.

The fabrication process of the test structures (Fig. 11) is as follows: (a) 2-cm^2 silicon-on-insulator (SOI) die was prepared. The thicknesses of the device layer, buried oxide layer and handling layer were 14.5 μm, 1.3 μm and 610 μm, respectively. The sample was cleaned with ammonia hydrogen peroxide (APM) and HF. (b) A 1-μm thick photo resist (JSR 7790G) was coated on the sample. It was patterned by laser lithography system (Heidelberg DWL66+), and etched using a deep reactive ion etching machine (SPTS MUC21 ASE-Pegasus). The
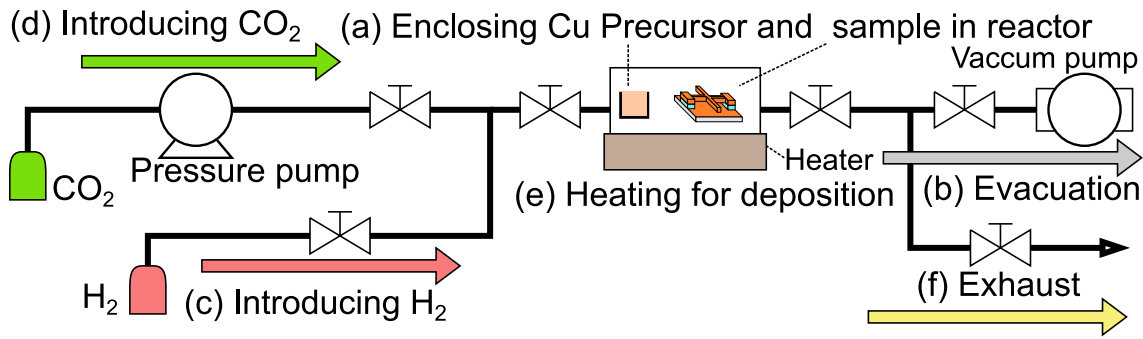
Fig. 12. Schematic of our supercritical fluids deposition (SCFD) system and its deposition procedure.
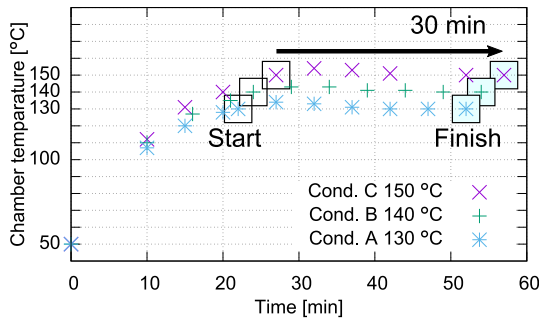

Fig. 13. Temperature control sequence in the SCFD process.

Fig. 14. Optical images of drop-in test structure before-and-after SCFD.

IV. EXPERIMENTAL RESULTS

Fig. 14 shows the images of the samples in the chamber before and after SCFD. The Cu film was clearly deposited through our SCFD process. The fabricated drop-in test structure chip was small enough to be placed with the main sample in the chamber. It also shows that there is no vacant area to enlarge the size of the drop-in test structure chip in the chamber. Therefore, the design of test structures was strictly limited to 5×10-mm$\square$.

We measured the actual dimensions of the fabricated samples. From the optical images, the measured shrinkage of arm width was 0.6 μm. Because the utilized samples were on the same die through the fabrication, the shrinkage of the arm width was identical between the samples utilized in all three conditions. Then, e_a was fixed to -0.6 μm in the following analysis. The thickness of the SCFD Cu film was measured through cross-sectional scanning electron microscopic images, and were obtained as 60, 70, and 100 nm for conditions A, B, and C, respectively. Fig. 15 presents the structure before and after SCFD and overlaid images to measure the displacement. The figure shows that the pointer clearly turned counterclockwise after SCFD. Our test structure has 20-μm-pitch scales, which were also utilized for alignment marks for precise overlaying.

Marker points in Fig. 16 present the measured displacements before and after SCFD. All pointers turned counterclockwise in conditions A, B, and C, indicating that the SCFD Cu films deposited under the adopted conditions possessed tensile stress. The displacements decreased with the designed width of arm w_a as predicted in Eq. (17). The displacements in condition A were too small to accurately measure the difference. The stress sensor of $w_a = 5.5$ μm in condition A did not move; this is due to the sticking phenomenon. The largest displacement was obtained in condition C, followed by conditions B and A. This does not directly imply that the SCFD Cu film in

etched sample was cleaned with oxygen plasma to remove the remaining resist. After device layer patterning, defect lines were scribed in the sample die by a laser stealth dicing machine (DISCO DFL7340). (c) The sample was cleaned with APM. The cantilever test structure was released using a vapor HF system (Idonus VPE200 Vapor Phase HF Etcher). After release, the die was divided into 5×10-mm$\square$ chips by using pre-scribed defect lines. (d) SiO$_2$, TiO$_2$ and Ru films as adhesion layers were deposited on released cantilevers using an ALD system (Oxford Instruments FlexAL). The thickness values of SiO$_2$, TiO$_2$ and Ru were 20 nm, 5 nm and 10 nm, respectively. The top adhesion layer was Ru. (e) Cu film was deposited with SCFD.

SCFD was performed using our batch-type SCFD system reported in [36], as shown in Fig. 12. Deposition procedures were as follows: (a) we enclosed samples and Cu precursor in the reactor. We utilized bis-(2,2,6,6-tetramethyl-3,5-heptanedionato)copper(II) [38] as precursor. The amount of precursor was 10 mg (0.002 mol/L). (b) The reactor was evacuated. (c) 1 MPa (0.39 mol/L) H$_2$ (p_{IH_2}) was introduced at 50 °C. (d) After the introduction of CO$_2$, the total pressure was 12 MPa at 50 °C. (e) Then, the temperature of the chamber was increased to T_r and held constant during t_r as shown in Fig. 13. (f) After finishing the SCFD, the chamber was cooled down and exhausted.

In our experiments, deposition time t_r was fixed at 30 min under all conditions, as shown in Fig. 13. Deposition temperatures for conditions A , B and C were 130, 140 and 150 °C, respectively. A comparison between results of the conditions A, B and C will provide dependence of residual stress in the SCFD Cu film on the deposition temperature.
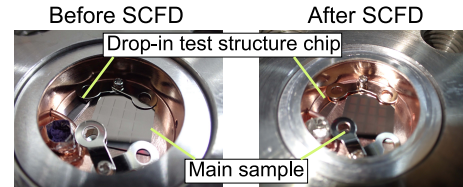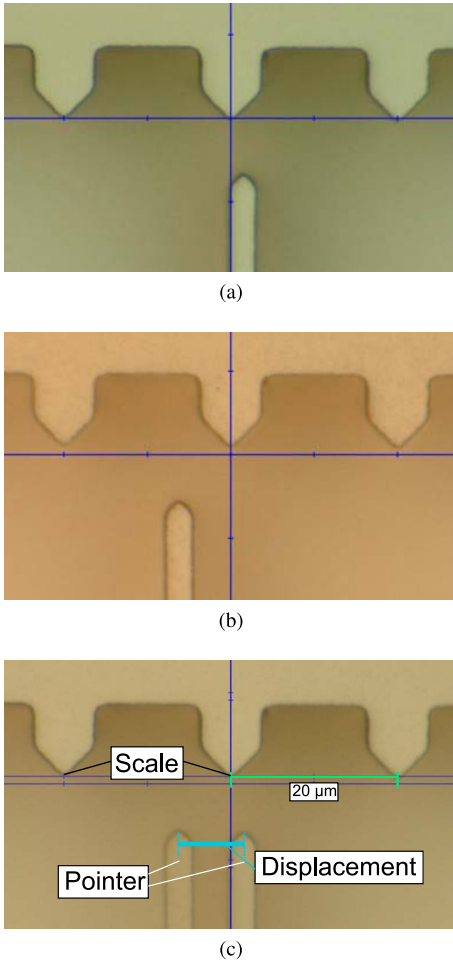
(a)

(b)

(c)

Fig. 15.   Optical image of displacements of pointer (a) before SCFD, (b) after SCFD and (c) composition between both cases.
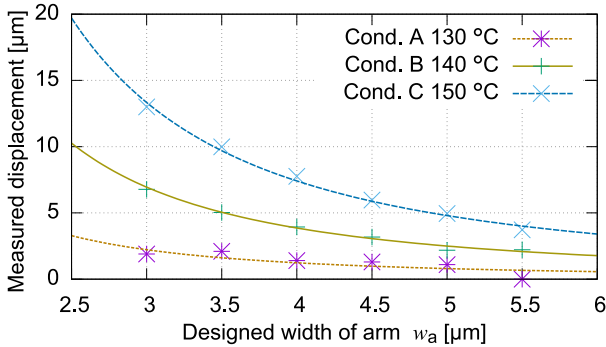

Fig. 16.   Points and lines show measurement results and theoretical predictions according to Eq. (17) with extracted material parameters, respectively.

condition C had a larger residual stress than in conditions A and B. As the utilized chips were diced from the same SOI die, structure-related parameters, such as β and e'_a (Eq. (17)), were common in all conditions. Therefore, the difference in displacements between the conditions reflects α. It depends not only on residual stress in the Cu film, σ_{FUT}, but also on thickness t_{FUT}, as Eq. (18). As mentioned earlier and in Table I, thickness of the deposited film increased in the order of conditions A to C.

TABLE I
PARAMETERS AND OBTAINED VARIANCE USED FOR CURVE FITTING BY EQ. (17) IN FIG. 16. σ_{FUT} IS CALCULATED FROM α USING EQ. (18)

Cond.	t_{FUT} [nm]	e_a[µm]	β [µm]	α [µm²]	σ_{FUT} [MPa]
A	60	-0.6	2.5	0.8	67
B	70	-0.6	2.5	2.5	160
C	100	-0.6	2.5	4.8	220

To prevent the influence of thickness and obtain the residual stress value, the w_a vs. d_p curve was fitted using Eq. (17). The fitted curves are shown in Fig. 16. The obtained values of variances and utilized parameters are shown in Table I. The value of β was assumed to be identical in all conditions because it was derived from the shape of the fabricated arm, and all samples were fabricated on the same die. Then, $\beta = 3.5\,\mu m$ was obtained from the fitting result in condition C and was adopted in conditions A and B. The residual stress values σ_{FUT} were calculated from α using Eq. (18). In the analysis, the Si elastic module E_{Si} and Poisson's ratio ν_{Si} were set to 170 GPa and 0.28 from a material table, respectively. Then, we obtained $\sigma_{FUT} = 67$ MPa in condition A, $\sigma_{FUT} = 160$ MPa in condition B, and $\sigma_{FUT} = 220$ MPa in condition C. The estimated stress values indicate that low-temperature condition suppresses residual stress. These values of residual stress were close to those in sputtered Cu films [24], and therefore our estimation may not be far from an actual scenario.

V. CONCLUSION

Our proposed free-standing rotating beam structure was demonstrated to be useful for directly visualizing and measuring the residual stress of thin films. The small chip size is suitable for experimental conformal deposition system development. Structural analysis of our stress sensor revealed an equation to estimate the residual stress value from the measurement results of several sensors with different arm lengths. The drop-in test structure chip containing six stress sensors is very small ($5 \times 10\,mm^2$), and the chip can thus be placed adjacent to the main sample in a small experimental chamber. As a demonstration, Cu SCFDs with three temperature conditions were performed, and the proposed test structures worked successfully. The results of residual stress in the SCFD Cu film indicated the dependence of the stress characteristics on the deposition temperature.

REFERENCES

[1] F. Marty *et al.*, "Advanced etching of silicon based on deep reactive ion etching for silicon high aspect ratio microstructures and three-dimensional micro- and nanostructures," *Microelectron. J.*, vol. 36, no. 7, pp. 673–677, 2005.

[2] C. F. Herrmann *et al.*, "Alternative dielectric films for RF MEMS capacitive switches deposited using atomic layer deposited Al_2O_3/ZnO alloys," *Sensors Actuators A Phys.*, vol. 135, no. 1, pp. 262–272, 2007.

[3] M. Bakri-Kassem and R. R. Mansour, "Linear bilayer ALD coated MEMS varactor with high tuning capacitance ratio," *J. Microelectromech. Syst.*, vol. 18, no. 1, pp. 147–153, 2009.

[4] J. L. Yeh, H. Jiang, H. P. Neves, and N. C. Tien, "Copper-encapsulated silicon micromachined structures," *J. Microelectromech. Syst.*, vol. 9, no. 3, pp. 281–287, 2000.

[5] Y. Shacham-Diamand, T. Osaka, Y. Okinaka, A. Sugiyama, and V. Dubin, "30 Years of electroless plating for semiconductor and polymer micro-systems," *Microelectron. Eng.*, vol. 132, pp. 35–45, Jan. 2015.

[6] P. C. Andricacos, C. Uzoh, J. O. Dukovic, J. Horkans, and H. Deligianni, "Damascene copper electroplating for chip interconnections," *IBM J. Res. Develop.*, vol. 42, no. 5, pp. 567–574, 1998.

[7] J. M. Blackburn, D. P. Long, A. Cabanas, and J. J. Watkins, "Deposition of conformal copper and nickel films from supercritical carbon dioxide." *Science*, vol. 294, no. 5540, pp. 141–145, 2001.

[8] M. Kubota *et al.*, "A 50 nm-wide 5m-deep copper vertical gap formation method by a gap-narrowing post-process with supercritical fluid deposition for pirani gauge operating over atmospheric pressure," in *Proc. IEEE MEMS*, 2012, pp. 204–207.

[9] A. G. Evans, M. D. Drory, and M. S. Hu, "The cracking and decohesion of thin films," *J. Mater. Res.*, vol. 3, no. 5, pp. 1043–1049, 1988.

[10] T. Kitamura, H. Hirakata, and T. Itsuji, "Effect of residual stress on delamination from interface edge between nano-films," *Eng. Fracture Mech.*, vol. 70, no. 15, pp. 2089–2101, 2003.

[11] G. G. Stoney, "The tension of metallic films deposited by electrolysis," *Proc. Roy. Soc. A Math. Phys. Eng. Sci.*, vol. 82, no. 553, pp. 172–175, 1909.

[12] G. Abadias *et al.*, "Review article: Stress in thin films and coatings: Current status, challenges, and prospects," *J. Vac. Sci. Technol. A Vac. Surfaces Films*, vol. 36, no. 2, 2018, Art. no. 020801.

[13] A. J. Wilkinson and T. B. Britton, "Strains, planes, and EBSD in materials science," *Mater. Today*, vol. 15, no. 9, pp. 366–376, 2012.

[14] X. Song *et al.*, "Residual stress measurement in thin films at sub-micron scale using focused ion beam milling and imaging," *Thin Solid Films*, vol. 520, no. 6, pp. 2073–2076, 2012.

[15] A. R. Behera, H. Shaik, G. M. Rao, and R. Pratap, "A technique for estimation of residual stress and young's modulus of compressively stressed thin films using microfabricated beams," *J. Microelectromech. Syst.*, vol. 28, no. 6, pp. 1039–1054, 2019.

[16] B. van Drieënhuizen, J. Goosen, P. French, and R. Wolffenbuttel, "Comparison of techniques for measuring both compressive and tensile stress in thin films," *Sensors Actuators A Phys.*, vols. 37–38, pp. 756–765, Jun.–Aug. 1993.

[17] A. B. Horsfall *et al.*, "Direct measurement of residual stress in sub-micron interconnects," *Semicond. Sci. Technol.*, vol. 18, no. 11, pp. 992–996, 2003.

[18] C. J. Wilson *et al.*, "A NEMS-based sensor to monitor stress in deep sub-micron Cu/Low-k interconnects," *Semicond. Sci. Technol.*, vol. 24, no. 11, 2009, Art. no. 115018.

[19] S. Smith *et al.*, "Fabrication and measurement of test structures to monitor stress in SU-8 films," *IEEE Trans. Semicond. Manuf.*, vol. 25, no. 3, pp. 346–354, Aug. 2012.

[20] X. Zhang, T. Y. Zhang, and Y. Zohar, "Measurements of residual stresses in thin films using micro-rotating-structures," *Thin Solid Films*, vol. 335, nos. 1–2, pp. 97–105, 1998.

[21] M. Kasbari *et al.*, "Metallization local stress monitoring in industrial semiconductor processes," in *Proc. Int. Workshop Stress Induced Phenom. Metallization*, vol. 945, 2007, pp. 21–26.

[22] R. R. Reddy, Y. Okamoto, and Y. Mita, "An on-chip micromachined test structure to study the tribological behavior of Deep-RIE MEMS sidewall surfaces," *IEEE Trans. Semicond. Manuf.*, vol. 33, no. 2, pp. 187–195, May 2020.

[23] A. C. Adams, F. B. Alexander, C. D. Capio, and T. E. Smith, "Characterization of plasma' deposited silicon dioxide," *J. Electrochem. Soc.*, vol. 128, no. 7, pp. 1545–1551, 1981.

[24] T. Hanabusa, K. Kusaka, and O. Sakata, "Residual stress and thermal stress observation in thin copper films," *Thin Solid Films*, vol. 459, nos. 1–2, pp. 245–248, 2004.

[25] M. Nahar, N. Rocklein, M. Andreas, G. Funston, and D. Goodner, "Stress modulation of titanium nitride thin films deposited using atomic layer deposition," *J. Vac. Sci. Technol. A Vac. Surfaces Films*, vol. 35, no. 1, 2017, Art. no. 01B144.

[26] N. Usami, E. Ota, A. Higo, T. Momose, and Y. Mita, "Area-selective Cu film growth on TiN and SiO_2 by supercritical fluid deposition," *IEEJ Trans. Sensors Micromach.*, vol. 140, no. 1, pp. 31–36, 2020.

[27] D. P. Long, J. M. Blackburn, and J. J. Watkins, "Chemical fluid deposition: A hybrid technique for low-temperature metallization," *Adv. Mater.*, vol. 12, no. 12, pp. 913–915, 2000.

[28] E. Kondoh and H. Kato, "Characteristics of copper deposition in a supercritical CO2fluid," *Microelectron. Eng.*, vol. 64, nos. 1–4, pp. 495–499, 2002.

[29] A. H. Romang and J. J. Watkins, "Supercritical fluids for the fabrication of semiconductor devices: Emerging or missed opportunities?" *Chem. Rev.*, vol. 110, no. 1, pp. 459–478, 2010.

[30] A. Cabañas, D. P. Long, and J. J. Watkins, "Deposition of gold films and nanostructures from supercritical carbon dioxide," *Chem. Mater.*, vol. 16, no. 10, pp. 2028–2033, 2004.

[31] M. Watanabe *et al.*, "Conformal copper coating of true three-dimensional through-holes using supercritical carbon dioxide," *Jpn. J. Appl. Phys.*, vol. 51, no. 5, 2012, Art. no. 05EA01.

[32] E. Kondoh and J. Fukuda, "Deposition kinetics and narrow-gap-filling in Cu thin film growth from supercritical carbon dioxide fluids," *J. Supercritical Fluids*, vol. 44, no. 3, pp. 466–474, 2008.

[33] C. F. Karanikas, H. Li, J. J. Vlassak, and J. J. Watkins, "Quantitative interfacial energy measurements of adhesion-promoted thin copper films by supercritical fluid deposition on barrier layers," *J. Eng. Mater. Technol.*, vol. 132, no. 2, 2010, Art. no. 021014.

[34] M. Rasadujjaman, M. Watanabe, H. Sudoh, H. Machida, and E. Kondoh, "Supercritical fluid chemical deposition of Cu in Ru and TiN-lined deep nanotrenches using a new Cu(I) amidinate precursor," *Microelectron. Eng.*, vol. 137, no. 1, pp. 32–36, 2015.

[35] B. Giroire *et al.*, "A comparative study of copper thin films deposited using magnetron sputtering and supercritical fluid deposition techniques," *Thin Solid Films*, vol. 643, pp. 53–59, Dec. 2017.

[36] N. Usami, E. Ota, T. Momose, A. Higo, and Y. Mita, "Influence of pre-treatment on the adhesion quality of super-critical-fluid-deposited (SCFD) Cu film on Si," *Sensors Mater.*, vol. 31, no. 8, pp. 2481–2496, 2019.

[37] N. Usami, E. Ota, A. Higo, T. Momose, and Y. Mita, "Drop-in test structure chip to visualize residual stress of ru/cu film grown by atomic layer deposition and supercritical fluid deposition," in *Proc. IEEE ICMTS*, 2020, pp. 1–4.

[38] T. Momose *et al.*, "Solubility of bis-(2,2,6,6-tetramethyl-3,5-heptanedionato)copper(II) in mixed supercritical CO_2 and H_2 systems for application in supercritical fluid deposition of Cu," *J. Supercritical Fluids*, vol. 105, pp. 193–200, Oct. 2015.